

Mass measurements show slowdown of rapid proton capture process at waiting-point nucleus ^{64}Ge

Received: 14 June 2022

Accepted: 24 March 2023

Published online: 1 May 2023

 Check for updates

X. Zhou^{1,2}, M. Wang^{1,2}✉, Y. H. Zhang^{1,2}✉, Yu. A. Litvinov^{1,3}✉, Z. Meisel⁴, K. Blaum⁵, X. H. Zhou^{1,2}, S. Q. Hou^{1,2,6}, K. A. Li¹, H. S. Xu^{1,2}, R. J. Chen^{1,3}, H. Y. Deng^{1,2}, C. Y. Fu¹, W. W. Ge¹, J. J. He⁷, W. J. Huang^{1,8}, H. Y. Jiao^{1,2}, H. F. Li^{1,2}, J. G. Li¹, T. Liao^{1,2}, S. A. Litvinov^{1,3}, M. L. Liu¹, Y. F. Niu⁹, P. Shuai¹, J. Y. Shi^{1,2}, Y. N. Song^{1,2}, M. Z. Sun¹, Q. Wang^{1,2}, Y. M. Xing¹, X. Xu¹, F. R. Xu¹⁰, X. L. Yan¹, J. C. Yang^{1,2}, Y. Yu^{1,2}, Q. Yuan¹⁰, Y. J. Yuan^{1,2}, Q. Zeng¹¹, M. Zhang^{1,2} & S. Zhang¹⁰

X-ray bursts are among the brightest stellar objects frequently observed in the sky by space-based telescopes. A type-I X-ray burst is understood as a violent thermonuclear explosion on the surface of a neutron star, accreting matter from a companion star in a binary system. The bursts are powered by a nuclear reaction sequence known as the rapid proton capture process (rp process), which involves hundreds of exotic neutron-deficient nuclides. At so-called waiting-point nuclides, the process stalls until a slower β^+ decay enables a bypass. One of the handful of rp process waiting-point nuclides is ^{64}Ge , which plays a decisive role in matter flow and therefore the produced X-ray flux. Here we report precision measurements of the masses of ^{63}Ge , $^{64,65}\text{As}$ and $^{66,67}\text{Se}$ —the relevant nuclear masses around the waiting-point ^{64}Ge —and use them as inputs for X-ray burst model calculations. We obtain the X-ray burst light curve to constrain the neutron-star compactness, and suggest that the distance to the X-ray burster GS 1826–24 needs to be increased by about 6.5% to match astronomical observations. The nucleosynthesis results affect the thermal structure of accreting neutron stars, which will subsequently modify the calculations of associated observables.

Type-I X-ray bursts occur on surfaces of neutron stars accreting hydrogen- and helium-rich matter from a companion star in a stellar binary system¹. The accreted fuel material is accumulated for hours to days on the surface before igniting and burning explosively for 10 to

100 s, causing a bright X-ray burst. Such objects are routinely observed with modern telescopes and belong to the brightest exasolar objects². The burst is powered by a sequence of nuclear reactions termed the rapid proton capture nucleosynthesis process (rp process)³, which is

¹CAS Key Laboratory of High Precision Nuclear Spectroscopy, Institute of Modern Physics, Chinese Academy of Sciences, Lanzhou, China. ²School of Nuclear Science and Technology, University of Chinese Academy of Sciences, Beijing, China. ³GSI Helmholtzzentrum für Schwerionenforschung, Darmstadt, Germany. ⁴Institute of Nuclear and Particle Physics, Department of Physics and Astronomy, Ohio University, Athens, OH, USA.

⁵Max-Planck-Institut für Kernphysik, Heidelberg, Germany. ⁶NuGrid Collaboration, <http://www.nugridstars.org>. ⁷Key Laboratory of Beam Technology of Ministry of Education, College of Nuclear Science and Technology, Beijing Normal University, Beijing, China. ⁸Advanced Energy Science and Technology Guangdong Laboratory, Huizhou, China. ⁹School of Nuclear Science and Technology, Lanzhou University, Lanzhou, China. ¹⁰State Key Laboratory of Nuclear Physics and Technology, School of Physics, Peking University, Beijing, China. ¹¹School of Nuclear Science and Engineering, East China University of Technology, Nanchang, China. ✉e-mail: wangm@impcas.ac.cn; yhzhang@impcas.ac.cn; y.litvinov@gsi.de

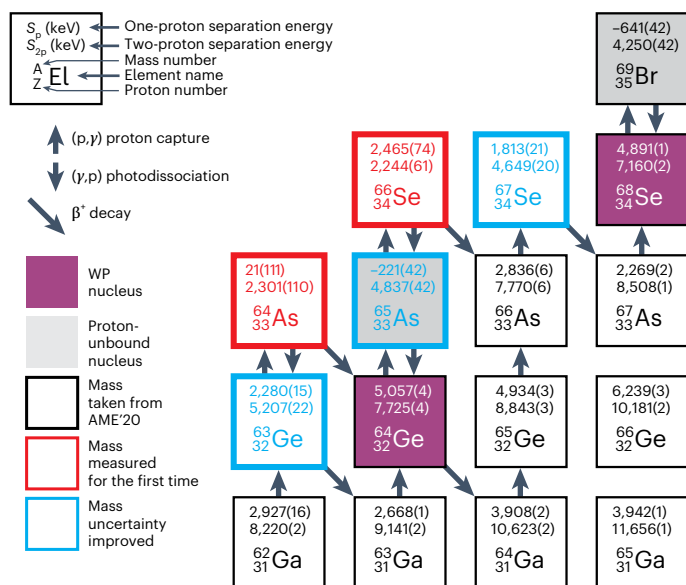


Fig. 1 Nuclear chart around the rp process WP ^{64}Ge . The nuclides are organized according to neutron (horizontally) and proton (vertically) numbers. Nuclides whose masses were taken from the latest AME'20 database³⁶, whose masses were experimentally determined or whose mass uncertainties were improved in this work are indicated in black, red and blue colours, respectively. The one-proton (S_p) and two-proton (S_{2p}) separation energies (values expressed in keV) follow the same colour code. The pathway of the rp process nucleosynthesis is shown with the black arrows. The legend provides more details.

a sequence of proton captures and β^+ decays along the proton drip line (Fig. 1). This line defines the limit beyond which the nuclei are unbound with respect to proton emission⁴. Thus, to unveil the mechanisms of the rp process, the properties of very exotic neutron-deficient nuclei need to be known. However, the relevant nuclei are typically characterized by short half-lives and tiny production yields in nuclear reactions utilized in terrestrial laboratories, which makes their experimental investigation extremely challenging⁵.

Waiting-point (WP) nuclei on the rp process play a particularly important role^{6–14}. These are the nuclei where the fast proton capture reactions cannot energetically proceed further and the process stalls until a much slower β^+ decay enables a bypass. A sequential capture of two protons can, in some cases, allow the process to bridge the WP. The key quantities defining the matter flow are one-proton (S_p) and two-proton (S_{2p}) separation energies, which are derived from nuclear masses of the relevant nuclei (Methods).

Three long-lived WP nuclei beyond ^{56}Ni (proton number $Z = 28$), namely, ^{64}Ge ($Z = 32$), ^{68}Se ($Z = 34$) and ^{72}Kr ($Z = 36$), play a crucial role. Their long effective stellar lifetimes give rise to the observed tails in the burst light curve. Comparing the modelled light curve profiles with observations provides quantitative information about the corresponding stellar environments^{15–19}. The rp process first encounters the exotic ^{64}Ge nucleus, which has a β^+ half-life of 63.7(25) s (ref. 20) comparable with the overall X-ray burst duration. It is, therefore, decisive to constrain the matter flow through ^{64}Ge .

In this work, we present the high-precision measurements of masses of ^{63}Ge , $^{64,65}\text{As}$ and $^{66,67}\text{Se}$. With our new results, all the relevant separation energies around WP ^{64}Ge (Fig. 1) are precisely determined.

Experimental procedure

The nuclei of interest are extremely neutron deficient and have very short half-lives, spreading from 54.0(4.0) ms for ^{66}Se to 153.6(1.1) ms for ^{63}Ge (ref. 20) (Table 1). Such short-lived nuclides have to be produced at a specialized radioactive ion beam facility and promptly studied, which

requires ultrafast and—due to small production quantities—ultrasensitive and efficient measurement techniques.

The present experiment was conducted at the Heavy Ion Research Facility in Lanzhou in operation at the Institute of Modern Physics of the Chinese Academy of Sciences^{21,22}. Primary beams of ^{78}Kr were accelerated by a chain of machines (Fig. 2), including a sector-focusing cyclotron and a main cooler-storage ring (CSRm) operating as a heavy-ion synchrotron. Every 25 s, a new beam was extracted from the CSRm as a microsecond-long bunch of $^{78}\text{Kr}^{19+}$ ions at a relativistic energy of 460 AMeV and focused onto a 15-mm-thick beryllium target in front of the fragment separator (RIBLL2).

Radionuclides were produced through projectile fragmentation nuclear reaction. In this reaction type, in principle, all the nuclei that can be obtained by removing nucleons from the projectile nucleus can be created, although the production probability rapidly decreases with the number of removed nucleons²³. Owing to the high kinetic energies, the reaction fragments emerged from the target as fully stripped bare nuclei^{24,25}. The fragments of interest were separated in flight from the remaining primary beam and intense contaminants using RIBLL2, and finally injected into the experimental cooler-storage ring (CSRe).

The RIBLL2–CSRe system was set to a fixed central magnetic rigidity of $B\rho = mv\gamma/q = 5.528\text{ Tm}$, where γ stands for the relativistic Lorentz factor; v and m/q are the velocity and mass-to-charge ratio of ions, respectively. In our experiment, $q = Z$. CSRe is characterized by a relatively large momentum acceptance of $\pm 0.33\%$. However, due to the nuclear reaction process, the fragments have much broader momentum distributions. This setting was optimized for a mass-to-charge ratio of $m/q \approx 1.965$. A cocktail beam of various produced species, including ^{63}Ge , $^{64,65}\text{As}$ and $^{66,67}\text{Se}$, which match with RIBLL2–CSRe acceptance, was transmitted, injected and stored.

The spread of revolution times, $\Delta T/T$, of the stored ions with a mass-to-charge ratio difference, $\Delta(m/q)/(m/q)$, is given as²⁶

$$\frac{\Delta T}{T} = \alpha_p \frac{\Delta(m/q)}{(m/q)} + \left(\frac{\gamma^2}{\gamma_t^2} - 1 \right) \frac{\Delta v}{v}, \quad (1)$$

where $\Delta v/v$ is the velocity spread. The momentum compaction factor $\alpha_p = 1/\gamma_t^2$, where γ_t is the transition energy, is a machine parameter that depends on the ring lattice and ion optical tuning²⁷. According to equation (1), the ion's revolution time is directly proportional to its mass-to-charge ratio if the second term containing the velocity spread is made negligibly small. This is the basic equation of storage-ring mass spectrometry^{26,28}.

One of the ways to compensate for the inevitable velocity spread of secondary ions is to employ a special isochronous ion optical mode of the ring. In this mode, a faster particle with a given mass-to-charge ratio, m/q , revolves on a longer orbit in the ring, whereas a slower particle with the same m/q moves on a correspondingly shorter orbit, such that their revolution times are the same. The isochronous condition is fulfilled for particles that have energies corresponding to $\gamma = \gamma_t$. In this experiment, $\gamma_t = 1.352$. In the first order, this condition makes the second term on the right-hand side of equation (1) become zero. This is the basis for conventional isochronous mass spectrometry (IMS)^{29,30}.

However, the condition $\gamma = \gamma_t$ is fulfilled only for a small range of mass-to-charge ratios, namely, the isochronicity window, which features the maximum resolving power³¹. To attain high mass-resolving power in the entire range of nuclear species, we succeeded in measuring the velocity of every stored ion in addition to its revolution time³². This enabled us to correct for 'non-isochronicity' effects and led to dramatically boosted sensitivity, efficiency and precision. We named this technique $B\rho$ -defined IMS or $B\rho$ -IMS (refs. 33,34), which is applied here to measure previously unknown masses (Methods).

The revolution times were measured with a couple of dedicated time-of-flight (ToF) detectors³⁵ (Methods). The measured revolution

Table 1 | Experimental results for ^{63}Ge , $^{64,65}\text{As}$ and $^{66,67}\text{Se}$ nuclei

Atom	$T_{1/2}$ (ms)	Events	ME_{IMS} (keV)	ME_{AME20} (keV)	ΔME (keV)	S_p (keV)
^{63}Ge	153.6(1.1)	279	-46,978(15)	-46,921(37)	-57(40)	2,280(15)
^{64}As	69.0(1.4)	6	-39,710(110)	-39,530(200)#	-180(230)#	21(111)
^{65}As	130.3(0.6)	33	-46,806(42)	-46,937(85)	131(95)	-221(42)
^{66}Se	54(4)	20	-41,982(61)	-41,660(200)#	-320(210)#	2,465(74)
^{67}Se	133(4)	174	-46,549(20)	-46,580(67)	31(70)	1,813(21)

The following data are obtained from this work: the number of measured ions (Events), mass excess values (ME_{IMS}) and proton separation energies (S_p). The literature half-lives ($T_{1/2}$) are from the NUBASE'20 (ref. 20). ΔME ($ME_{\text{IMS}} - ME_{\text{AME20}}$) values are the differences from literature mass values (ME_{AME20}) taken from AME20³⁶. The symbol # indicates the extrapolated values in AME'20 (refs. 20,36).

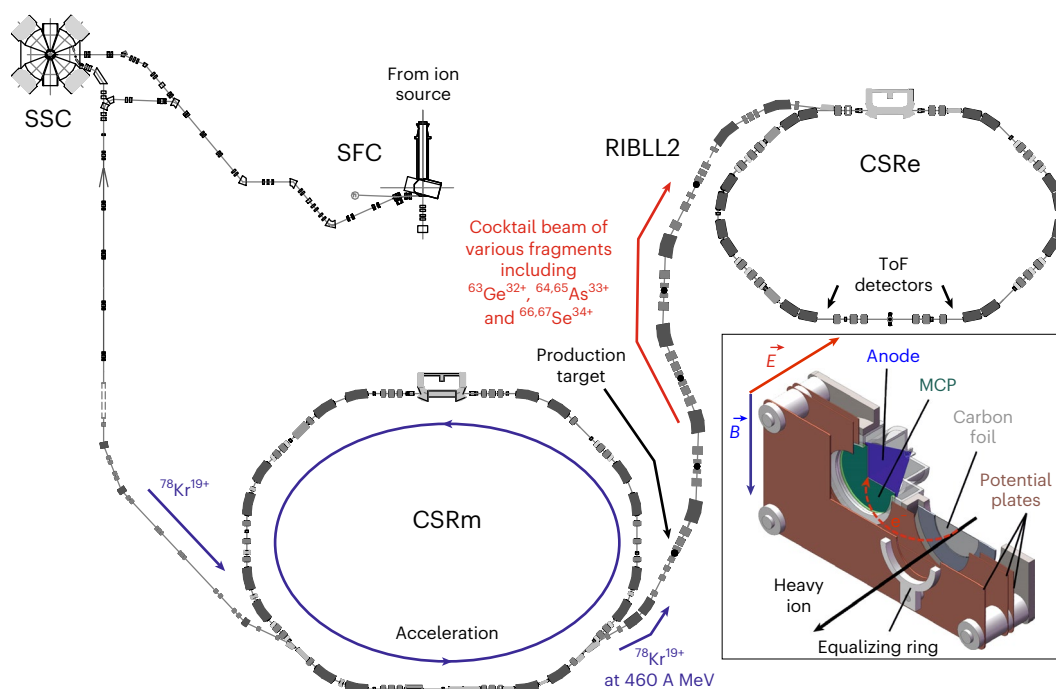


Fig. 2 | Schematic of the Heavy Ion Research Facility in Lanzhou. In this experiment, the primary beam of $^{78}\text{Kr}^{19+}$ was successively accelerated by the sector-focusing cyclotron (SFC) and heavy-ion synchrotron (CSRm) and then extracted to bombard the production target to produce exotic nuclei. Beams of various nuclear species including ^{63}Ge , $^{64,65}\text{As}$ and $^{66,67}\text{Se}$ were collected and separated with RIBLL2 and injected into CSRc, where the masses of the nuclei of interest were determined with high precision through the measurement of

their revolution times and velocities applying $B\rho$ -IMS spectrometry^{33,34}. The separated-sector cyclotron (SSC) was not used in this experiment. The inset shows a schematic of the ToF detector. The secondary electrons released from the carbon foil are guided by the crossed electrostatic and magnetic fields to the MCP. The electrostatic field E is produced by three potential plates, namely, carbon foil, MCP and equalizing ring, and the magnetic field B is produced by an external dipole magnet.

time spectrum is illustrated in Fig. 3a. It contains all the valid particles measured within the about two-week-long experiment. Nuclides of interest with unknown masses as well as those with well-known masses are indicated in different colours. Well-known mass values from the literature with uncertainties of $\sigma < 5$ keV have been used as calibrants (Fig. 3; blue peaks) to precisely determine the masses of ^{63}Ge , $^{64,65}\text{As}$ and $^{66,67}\text{Se}$ (Fig. 3; red peaks).

Masses of ^{63}Ge , $^{64,65}\text{As}$ and $^{66,67}\text{Se}$

The mass excess (in keV) is defined as $ME = m - A$, where m is the atomic mass (in atomic units with $u = 931,494.10242(28)$ keV c^{-2} (ref. 36)) and $A = Z + N$ is the mass number of the nucleus. The ME values determined in this work are given in Table 1, where we employ natural units with $c = \hbar = 1$. The numbers of measured ions (Events) are also listed. The literature half-lives ($T_{1/2}$) are from the 2020 NUBASE evaluation (ref. 20) and mass values (ME_{AME20}) are from the 2020 Atomic Mass Evaluation (AME20) (ref. 36). In addition to a compilation of all the experimentally

known masses, AME'20 provides extrapolated values for yet-unknown masses. Such extrapolations are indicated with the symbol # in the table.

It is striking that only six ions of the short-lived ^{64}As were detected, which corresponds to a rate of about three ions per week. Still, its mass could be determined with a relative mass uncertainty of $\delta m/m \approx 1.8 \times 10^{-6}$.

The mass excesses of ^{64}As and ^{66}Se were experimentally unknown. The new values of $ME(^{64}\text{As}) = -39,710(110)$ keV and $ME(^{66}\text{Se}) = -41,982(61)$ keV are 180(230) and 320(210) keV, respectively, more bound than the corresponding extrapolated values in AME'20 (refs. 20,36). The obtained proton separation energies are given in Table 1 and Fig. 1. The new, positive $S_p(^{64}\text{As}) = 21(111)$ keV indicates that this odd-odd nucleus might be proton bound.

The mass-to-charge ratios of $^{66}\text{Se}^{34+}$ and $^{33}\text{Cl}^{17+}$ ions are nearly the same. These ions cannot be resolved by their revolution times and are seen as a common revolution time peak at about 635.5 ns (Fig. 3a).

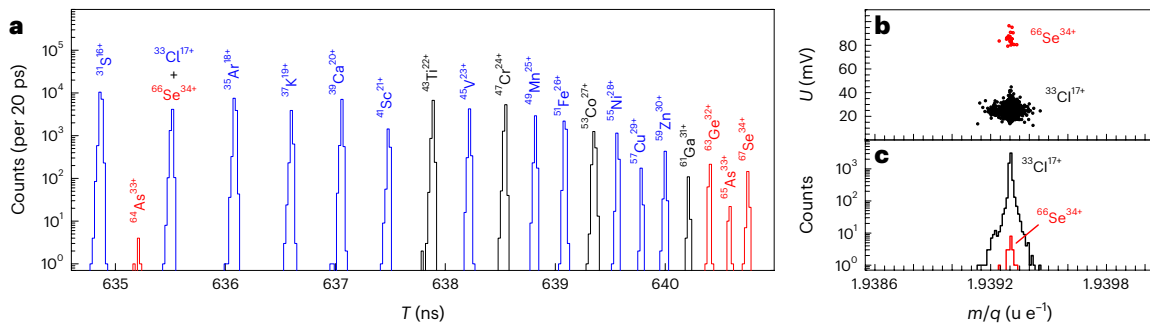


Fig. 3 | Experimental spectra. **a**, Measured revolution time spectrum. The nuclei whose masses were measured in this work are shown in red. Nuclides with well-known masses were used as references and are indicated in blue. The nuclides in black were not used as references due to possible isomeric contaminations or large mass uncertainty. **b**, Scatter plot of the charge-dependent parameter U ,

which reflects the mean number of secondary electrons released from the foil surface (equation (8)), for $^{37}\text{Cl}^{17+}$ and $^{66}\text{Se}^{34+}$ ions, see the peak at about 635.5 ns in **a**. The events belonging to each of the ion species can be clearly separated. **c**, Histogram of calculation with equation (7) involving the mass-to-charge ratios (m/q) of the peaks resolved in **b**, namely, $^{37}\text{Cl}^{17+}$ and $^{66}\text{Se}^{34+}$ ions.

Therefore, a special procedure was employed to determine the mass of ^{66}Se (Fig. 3b,c and Methods).

The uncertainties of the ME values of ^{63}Ge , ^{65}As and ^{67}Se were improved by more than a factor of two. The new ME value of ^{65}As is in agreement, within 1.4σ uncertainty, with our previous measurement^{37,38}. The previously known $S_p(^{65}\text{As}) = -90(85)$ keV is now replaced by $-221(42)$ keV, which firmly establishes this nucleus as proton unbound.

To check the reliability of the measured masses, we employed a standard procedure described in detail elsewhere^{39–44}. Each of the reference masses (i) was supposed, one by one, to be unknown, and its mass was redetermined by using the remaining reference nuclides as calibrants. The redetermined mass excesses ($ME_{\text{exp},i}$) and the corresponding statistical uncertainties ($\sigma_{\text{exp},i}$) were utilized to calculate the normalized χ_n defined as

$$\chi_n = \sqrt{\frac{1}{N_c} \sum_{i=1}^{N_c} \frac{[ME_{\text{exp},i} - ME_{\text{AME20},i}]^2}{\sigma_{\text{exp},i}^2 + \sigma_{\text{AME20},i}^2}}, \quad (2)$$

where N_c is the number of calibrants and $ME_{\text{AME20},i}$ and $\sigma_{\text{AME20},i}$ denote the mass excesses and 1σ uncertainties from AME'20, respectively^{20,36}. The calculated $\chi_n = 1.066$ is within the expected range of $\chi_n = 1 \pm 1/\sqrt{2N_c} = 1 \pm 0.139$ at the 1σ confidence level, indicating that no additional systematic errors need to be considered.

X-ray burst simulations

The impact of the new masses has been investigated through state-of-the-art multizone X-ray burst simulations. The accreting neutron-star system properties were selected to best reproduce the 2007 bursting epoch of the well-studied ‘clock burster’ GS 1826–24 (refs. 45–47). Methods provides the details. For the calculations, we replaced the corresponding nuclear masses in the AME'20 database³⁶ (indicated as AME'20 hereafter) with our new results obtained in this work (indicated as ‘Updated’).

The simulated X-ray burst light curves are shown in Fig. 4. The new nuclear masses, particularly the less bound ^{65}As and more bound ^{66}Se , result in a stalled rp process at the WP ^{64}Ge (Fig. 1). Single-zone calculations in another work⁴⁸ indicate that a slower flow reduces energy generation but preserves hydrogen to be burnt later in the burst, thus leading to longer bursts. We emphasize that the somewhat increased peak X-ray flux (Fig. 4) is not seen in single-zone calculations⁴⁸, and therefore, we speculate that this is related to the convective mixing of different burning layers.

The new distributions of the elements produced through the rp nucleosynthesis (‘ashes’) are also modified (Fig. 4, inset). The ash

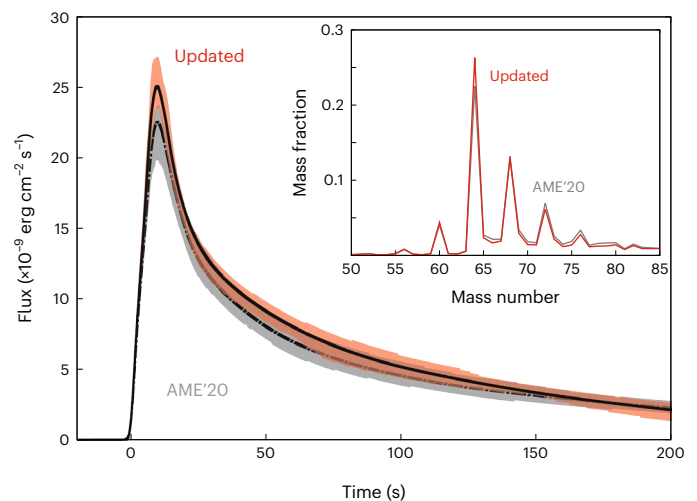


Fig. 4 | Calculated X-ray burst light curves. The baseline nuclear physics input is labelled as AME'20 (dash-dot line and grey band). The result with the nuclear masses determined in this work is marked as Updated (solid line and red band). The light curve bands correspond to 68% confidence intervals. The shown light curve bands have a nominal surface gravitational redshift of 1.42 and distance of 6.2 kpc applied. The inset shows the calculated mass fractions $X(A)$ as a function of mass number. These were obtained by averaging over envelope layers that no longer experienced hydrogen or helium burning, as described in other work^{52,57,60}. The corresponding datasets can be found elsewhere⁶¹.

abundances of Urca nuclides are particularly notable^{49,50}, which may impact the interpretation of model–observation comparisons for X-ray superbursts and neutron-star crust cooling^{51,52}, as well as of important electron-capture heating sources⁵³. Of these, we note that our new masses result in a 17% increase in the $A = 64$ ash mass fraction and 14% decrease in the $A = 65$ ash mass fraction, which is consistent with the rp process stalling near ^{64}Ge . The former will result in increased electron-capture heating, whereas the latter will result in reduced Urca cooling, overall implying a somewhat warmer accreted neutron-star crust.

The X-ray burst luminosity measured by a telescope is directly proportional to the emitted light flux and inversely proportional to the square of the distance (d^2) and the surface gravitational redshift $(1+z)^2$ of the burster, corrected by the electromagnetic wave transport efficiency^{54–56}. Our new light curve enables us to set new constraints on the optimal d and $(1+z)$ parameters (Methods), which fit the observational data. The results are shown in Fig. 5a. The increased peak luminosity

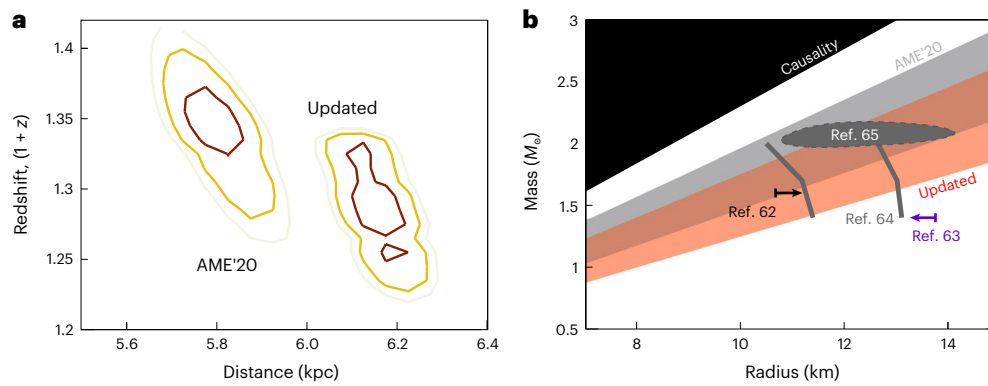


Fig. 5 | Constraints on neutron-star parameters. a, Surface gravitational redshift versus distance of the source GS 1826–24 obtained through a comparison of the modelled light curves (Fig. 4) and the observational data from the year 2007 bursting epoch (Methods). The colours indicate 68% (red), 90% (yellow) and 95% (grey) confidence intervals. Two regions correspond to results using previously known masses (AME'20) and if our new masses are included

(Updated). **b**, Neutron-star mass (M_{NS}) versus radius (R_{NS}) constraints calculated from the $(1+z)$ 95% confidence intervals shown in **a**. The limits for neutron-star compactness determined using other astrophysical observables are also shown, that is, from individual merger events^{62,63}, quiescent low-mass X-ray binaries⁶⁴ and pulsar radio timing combined with X-ray pulse-profile modelling⁶⁵, along with the unphysical region excluded by causality⁶⁶ (shown in black).

requires distance d to be increased by ~ 0.4 kpc from about 5.8 kpc to about 6.2 kpc. The rp process stalled at ^{64}Ge leads to extended hydrogen burning in the light curve, extending the burst tail. As a consequence, the modelled light curve needs to be less time dilated, thus reducing $(1+z)$. The shown uncertainties are due to burst-to-burst variations in the calculated light curve. Due to computer-power-intensive calculations, only the mean mass values are considered in the simulations and not the uncertainties of the mass values, the net effect of which can be imagined if considering the deviations listed in Table 1.

The constraints on $(1+z)$ can be further converted into limits on neutron-star compactness ($M_{\text{NS}}/R_{\text{NS}}$) following the approach introduced elsewhere⁵⁷. The general relativistic neutron-star mass M_{GR} and radius R_{GR} are determined by $(1+z) = 1/\sqrt{1-2GM_{\text{GR}}/(R_{\text{GR}}c^2)}$, where c is the speed of light and G is the gravitational constant. For the choice that the Newtonian mass is equal to the general relativistic mass, $M_{\text{NS}} = M_{\text{GR}}$, then $R_{\text{GR}} = \sqrt{(1+z)}R_{\text{NS}}$. The compactness constraints corresponding to the 95% confidence intervals (Fig. 5a) are shown in Fig. 5b, along with mass and radius constraints from other observational probes and theoretical limits. Our results suggest a less-compact neutron star in GS 1826–24, which will require an adjustment of the equation of state for dense matter⁵⁸. It should be noted that several model uncertainties contribute to this compactness constraint, for example, possible alterations of the light curve due to flame spreading. As such, it is most interesting to compare the relative change in compactness bands due to a change in nuclear physics, as opposed to focusing on the absolute constraints themselves.

Outlook

Previously, compatibility with zero proton separation energy in ^{65}As used in a single-zone model showed that ^{64}Ge is not a significant WP nucleus in the rp process³⁷. Within the framework of the employed multizone X-ray burst model, we arrive here at a different result. In this context, we note that although the uncertainties due to nuclear masses are largely reduced through this work, the ones related to astrophysical simulations remain. This requires further developments, for example, by accounting for three-dimensional convection⁵⁹.

Systematic studies of the sensitivity of single-zone X-ray burst simulations to mass uncertainties⁴⁸ concluded that masses of only a few nuclei have a major effect, with ^{65}As and ^{66}Se causing the largest impact. The masses for both nuclei were measured in this work. A consequence is an increased importance to constrain nuclear physics around the following ^{68}Se and ^{72}Kr WPs, where the mass measurements of the relevant nuclides are not yet accomplished.

Online content

Any methods, additional references, Nature Portfolio reporting summaries, source data, extended data, supplementary information, acknowledgements, peer review information; details of author contributions and competing interests; and statements of data and code availability are available at <https://doi.org/10.1038/s41567-023-02034-2>.

References

- Joss, P. C. X-ray bursts and neutron-star thermonuclear flashes. *Nature* **270**, 310–314 (1977).
- Galloway, D. K. et al. The multi-instrument burst archive (MINBAR). *Astrophys. J. Suppl. Ser.* **249**, 32 (2020).
- Wallace, R. K. & Woosley, S. E. Explosive hydrogen burning. *Astrophys. J. Suppl. Ser.* **45**, 389–420 (1981).
- Thoennessen, M. Reaching the limits of nuclear stability. *Rep. Prog. Phys.* **67**, 1187–1232 (2004).
- Geissel, H., Münzenberg, G. & Riisager, K. Secondary exotic nuclear beams. *Annu. Rev. Nucl. Part. Sci.* **45**, 163–203 (1995).
- van Wormer, L., Görres, J., Iliadis, C., Wiescher, M. & Thielemann, F.-K. Reaction rates and reaction sequences in the rp-process. *Astrophys. J.* **432**, 326–350 (1994).
- Schatz, H. et al. rp-process nucleosynthesis at extreme temperature and density conditions. *Phys. Rep.* **294**, 167–263 (1998).
- Koike, O., Hashimoto, M., Arai, K. & Wanajo, S. Rapid proton capture on accreting neutron stars—effects of uncertainty in the nuclear process. *Astron. Astrophys.* **342**, 464–473 (1999).
- Schatz, H. et al. End point of the rp process on accreting neutron stars. *Phys. Rev. Lett.* **86**, 3471–3474 (2001).
- Clement, R. R. C. et al. Sensitivities of rp-process calculations to nuclear mass uncertainties. *Nucl. Phys. A* **718**, 617–619 (2003).
- Fisker, J. L., Schatz, H. & Thielemann, F.-K. Explosive hydrogen burning during type I X-ray bursts. *Astrophys. J. Suppl. Ser.* **174**, 261–276 (2008).
- Parikh, A., José, J., Sala, G. & Iliadis, C. Nucleosynthesis in type I X-ray bursts. *Prog. Part. Nucl. Phys.* **69**, 225–253 (2013).
- Lam, Y. H. et al. Reaction rates of $^{64}\text{Ge}(p, \gamma)^{65}\text{As}$ and $^{65}\text{As}(p, \gamma)^{66}\text{Se}$ and the extent of nucleosynthesis in type I X-ray bursts. *Astrophys. J.* **818**, 78 (2016).
- Meisel, Z., Deibel, A., Keek, L., Shternin, P. & Elfriz, J. Nuclear physics of the outer layers of accreting neutron stars. *J. Phys. G: Nucl. Part. Phys.* **45**, 093001 (2018).

15. Schatz, H. & Rehm, K. E. X-ray binaries. *Nucl. Phys. A* **777**, 601–622 (2006).
16. Heger, A., Cumming, A., Galloway, D. K. & Woosley, S. E. Models of type I X-ray bursts from GS 1826–24: a probe of rp-process hydrogen burning. *Astrophys. J.* **671**, L141–L144 (2007).
17. Meisel, Z. Consistent modeling of GS 1826–24 X-ray bursts for multiple accretion rates demonstrates the possibility of constraining rp-process reaction rates. *Astrophys. J.* **860**, 147 (2018).
18. Goodwin, A. J., Galloway, D. K., Heger, A., Cumming, A. & Johnston, Z. A Bayesian approach to matching thermonuclear X-ray burst observations with models. *Mon. Not. R. Astron. Soc.* **490**, 2228–2240 (2019).
19. Johnston, Z., Heger, A. & Galloway, D. K. Multi-epoch X-ray burst modelling: MCMC with large grids of 1D simulations. *Mon. Not. R. Astron. Soc.* **494**, 4576–4589 (2020).
20. Kondev, F. G., Wang, M., Huang, W. J., Naimi, S. & Audi, G. The NUBASE2020 evaluation of nuclear physics properties. *Chinese Phys. C* **45**, 030001 (2021).
21. Xia, J. W. et al. The heavy ion cooler-storage-ring project (HIRFL-CSR) at Lanzhou. *Nucl. Instrum. Meth. Phys. Res. A* **488**, 11–25 (2002).
22. Zhan, W. L. et al. Progress in HIRFL-CSR. *Nucl. Phys. A* **834**, 694–700 (2010).
23. Sümmerer, K. & Blank, B. Modified empirical parametrization of fragmentation cross sections. *Phys. Rev. C* **61**, 034607 (2000).
24. Scheidenberger, C. et al. Charge states of relativistic heavy ions in matter. *Nucl. Instrum. Meth. Phys. Res. B* **142**, 441–462 (1998).
25. Litvinov, Y. A. & Bosch, F. Beta decay of highly charged ions. *Rep. Prog. Phys.* **74**, 016301 (2011).
26. Franzke, B., Geissel, H. & Münzenberg, G. Mass and lifetime measurements of exotic nuclei in storage rings. *Mass Spectrom. Rev.* **27**, 428–469 (2008).
27. Steck, M. & Litvinov, Y. A. Heavy-ion storage rings and their use in precision experiments with highly charged ions. *Prog. Part. Nucl. Phys.* **115**, 103811 (2020).
28. Bosch, F., Litvinov, Y. A. & Stöhlker, T. Nuclear physics with unstable ions at storage rings. *Prog. Part. Nucl. Phys.* **73**, 84–140 (2013).
29. Hausmann, M. et al. First isochronous mass spectrometry at the experimental storage ring ESR. *Nucl. Instrum. Meth. Phys. Res. A* **446**, 569–580 (2000).
30. Hausmann, M. et al. Isochronous mass measurements of hot exotic nuclei. *Hyperfine Interact.* **132**, 289–295 (2001).
31. Zhang, Y. H., Litvinov, Y. A., Uesaka, T. & Xu, H. S. Storage ring mass spectrometry for nuclear structure and astrophysics research. *Phys. Scr.* **91**, 073002 (2016).
32. Zhou, X. et al. In-ring velocity measurement for isochronous mass spectrometry. *Phys. Rev. Accel. Beams* **24**, 042802 (2021).
33. Wang, M. et al. $B\rho$ -defined isochronous mass spectrometry: an approach for high-precision mass measurements of short-lived nuclei. *Phys. Rev. C* **106**, 051301 (2022).
34. Zhang, M. et al. $B\rho$ -defined isochronous mass spectrometry and mass measurements of ^{58}Ni fragments. *Eur. Phys. J. A* **59**, 27 (2023).
35. Mei, B. et al. A high performance time-of-flight detector applied to isochronous mass measurement at CSRe. *Nucl. Instrum. Meth. Phys. Res. A* **624**, 109–113 (2010).
36. Wang, M., Huang, W. J., Kondev, F. G., Audi, G. & Naimi, S. The AME 2020 atomic mass evaluation (II). Tables, graphs and references. *Chinese Phys. C* **45**, 030003 (2021).
37. Tu, X. L. et al. Direct mass measurements of short-lived $A=2Z-1$ nuclides ^{63}Ge , ^{65}As , ^{67}Se , and ^{71}Kr and their impact on nucleosynthesis in the rp process. *Phys. Rev. Lett.* **106**, 112501 (2011).
38. Tu, X. L. et al. Precision isochronous mass measurements at the storage ring CSRe in Lanzhou. *Nucl. Instrum. Meth. Phys. Res. A* **654**, 213–218 (2011).
39. Zhang, Y. H. et al. Mass measurements of the neutron-deficient ^{41}Ti , ^{45}Cr , ^{49}Fe , and ^{53}Ni nuclides: first test of the isobaric multiplet mass equation in fp -shell nuclei. *Phys. Rev. Lett.* **109**, 102501 (2012).
40. Yan, X. L. et al. Mass measurement of ^{45}Cr and its impact on the Ca–Sc cycle in X-ray bursts. *Astrophys. J. Lett.* **766**, L8 (2013).
41. Shuai, P. et al. Charge and frequency resolved isochronous mass spectrometry and the mass of ^{51}Co . *Phys. Lett. B* **735**, 327–331 (2014).
42. Xu, X. et al. Identification of the lowest $T=2$, $J^\pi=0^+$ isobaric analog state in ^{52}Co and its impact on the understanding of β -decay properties of ^{52}Ni . *Phys. Rev. Lett.* **117**, 182503 (2016).
43. Zhang, P. et al. High-precision Q_{EC} values of superallowed $0^+ \rightarrow 0^+$ β -emitters ^{46}Cr , ^{50}Fe and ^{54}Ni . *Phys. Lett. B* **767**, 20–24 (2017).
44. Xing, Y. M. et al. Mass measurements of neutron-deficient Y, Zr, and Nb isotopes and their impact on rp and vp nucleosynthesis processes. *Phys. Lett. B* **781**, 358–363 (2018).
45. Bildsten, L. Theory and observations of type I X-ray bursts from neutron stars. *AIP Conf. Proc.* **522**, 359–369 (2000).
46. Galloway, D. K., Munro, M. P., Hartman, J. M., Dimitrios, P. & Chakrabarty, D. Thermonuclear (Type I) X-ray bursts observed by the Rossi X-ray Timing Explorer. *Astrophys. J. Suppl. Ser.* **179**, 360–422 (2008).
47. Galloway, D. K., Goodwin, A. J. & Keek, L. Thermonuclear burst observations for model comparisons: a reference sample. *Pub. Astron. Soc. Aust.* **34**, E019 (2017).
48. Schatz, H. & Ong, W.-J. Dependence of X-ray burst models on nuclear masses. *Astrophys. J.* **844**, 139 (2017).
49. Schatz, H. et al. Strong neutrino cooling by cycles of electron capture and β^- decay in neutron star crusts. *Nature* **505**, 62–65 (2014).
50. Lau, R. et al. Nuclear reactions in the crusts of accreting neutron stars. *Astrophys. J.* **859**, 62 (2018).
51. Deibel, A., Meisel, Z., Schatz, H., Brown, E. F. & Cumming, A. Urca cooling pairs in the neutron star ocean and their effect on superbursts. *Astrophys. J.* **831**, 13 (2016).
52. Meisel, Z. & Deibel, A. Constraints on bygone nucleosynthesis of accreting neutron stars. *Astrophys. J.* **837**, 73 (2017).
53. Gupta, S., Brown, E. F., Schatz, H., Moller, P. & Kratz, K.-L. Heating in the accreted neutron star ocean: implications for superburst ignition. *Astrophys. J.* **662**, 1188–1197 (2007).
54. Fujimoto, M. Y. Angular distribution of radiation from low-mass X-ray binaries. *Astrophys. J.* **324**, 995–1000 (1988).
55. He, C.-C. & Keek, L. Anisotropy of X-ray bursts from neutron stars with concave accretion disks. *Astrophys. J.* **819**, 47 (2016).
56. Lam, Y. H. et al. The regulated NiCu cycles with the new $^{57}\text{Cu}(p,\gamma)^{58}\text{Zn}$ reaction rate and its influence on type I X-ray bursts: the GS 1826–24 clocked burster. *Astrophys. J.* **929**, 73 (2022).
57. Meisel, Z., Merz, G. & Medvid, S. Influence of nuclear reaction rate uncertainties on neutron star properties extracted from X-ray burst model-observation comparisons. *Astrophys. J.* **872**, 84 (2019).
58. Huth, S. et al. Constraining neutron-star matter with microscopic and macroscopic collisions. *Nature* **606**, 276–280 (2022).
59. Zingale, M., Malone, C. M., Nonaka, A., Almgren, A. S. & Bell, J. B. Comparisons of two- and three-dimensional convection in type I X-ray bursts. *Astrophys. J.* **807**, 60 (2015).
60. Cyburt, R. H. et al. Dependence of X-ray burst models on nuclear reaction rates. *Astrophys. J.* **830**, 55 (2016).
61. Zhou, X. et al. XRB_LightCurves_Ashes. Zenodo <https://zenodo.org/record/7427118#ZBD7WY8w2gQ> (2022).
62. Bauswein, A., Just, O., Janka, H.-T. & Stergioulas, N. Neutron-star radius constraints from GW 170817 and future detections. *Astrophys. J. Lett* **850**, L34 (2017).

63. Fattoyev, F. J., Piekarewicz, J. & Horowitz, C. J. Neutron skins and neutron stars in the multimessenger era. *Phys. Rev. Lett.* **120**, 172702 (2018).
64. Steiner, A. W. et al. Constraining the mass and radius of neutron stars in globular clusters. *Mon. Not. R. Astron. Soc.* **476**, 421–435 (2018).
65. Riley, T. E. et al. A NICER view of the massive pulsar PSR J0740+6620 informed by radio timing and XMM-Newton spectroscopy. *Astrophys. J. Lett.* **918**, L27 (2021).
66. Koranda, S., Stergioulas, N. & Friedman, J. L. Upper limits set by causality on the rotation and mass of uniformly rotating relativistic stars. *Astrophys. J.* **488**, 799–806 (1997).

Publisher's note Springer Nature remains neutral with regard to jurisdictional claims in published maps and institutional affiliations.

Open Access This article is licensed under a Creative Commons Attribution 4.0 International License, which permits use, sharing, adaptation, distribution and reproduction in any medium or format, as long as you give appropriate credit to the original author(s) and the source, provide a link to the Creative Commons license, and indicate if changes were made. The images or other third party material in this article are included in the article's Creative Commons license, unless indicated otherwise in a credit line to the material. If material is not included in the article's Creative Commons license and your intended use is not permitted by statutory regulation or exceeds the permitted use, you will need to obtain permission directly from the copyright holder. To view a copy of this license, visit <http://creativecommons.org/licenses/by/4.0/>.

© The Author(s) 2023

Methods

Nucleon separation energies

Energy required to remove one or several nucleons from a nucleus is termed the separation energy⁴. It is given by the difference in the mass of the parent atom and the sum of the masses of the removed nucleons and daughter atom. It is noted that the atomic electrons need to be taken into account. For instance, the proton separation energy, $S_p(Z, N)$, of a nucleus with Z protons and N neutrons is defined as

$$S_p(Z, N) = [m(Z - 1, N) + m_H] - m(Z, N), \quad (3)$$

where $m(Z, N)$ and $m(Z - 1, N)$ are the masses of the parent and daughter atoms, respectively, and m_H is the mass of the hydrogen atom. Correspondingly, the two-proton separation energy, S_{2p} , is given by

$$S_{2p}(Z, N) = [m(Z - 2, N) + 2m_H] - m(Z, N). \quad (4)$$

Other separation energies can be analogously constructed.

Revolution time measurement

The CSRe storage ring has a circumference of 128.8 m on the central orbit. The revolution times of stored ions were measured with a pair of identical ToF detectors installed 18 m apart in one of the straight sections of the CSRe (refs. 32,67–70) (Fig. 2).

Each detector was composed of a carbon foil, electrostatic potential electrodes and a set of microchannel plates (MCPs), directly inserted into the ultrahigh-vacuum environment of the storage ring, as well as Helmholtz coils placed outside the vacuum chamber^{35,71,72}. The self-supporting foil had a thickness of 20 $\mu\text{g cm}^{-2}$, corresponding to about 90 nm, and a diameter of 40 mm. A sketch of the detector is given in Fig. 2 (inset).

Each ion circulating in the ring successively passed through the foils of both TOF detectors at each revolution. Secondary electrons released from the surfaces of the foils were isochronously guided by the crossed electrostatic and weak magnetic fields to the MCP. The anode signal from the MCP was continuously digitized with 50 gigasamples per second. The measurement was triggered by the injection of fresh ions into the CSRe. The measurement time was 400 μs , corresponding to about 600 revolutions of ions in the ring.

On average, 36 ions were stored in the ring in each injection. The quantities of various ion species depended only on their production yields and transmission efficiencies. The digitized data were processed to determine all the passage times. To extract timing information independent from the signal amplitudes, a constant fractional discrimination algorithm³⁸ has been employed. All the timing signals were sorted and unambiguously assigned to individual ions. As the final result, for every stored ion, we obtained two trains of timing signals from two detectors. By fitting these time sequences, revolution time and velocity of every ion at every revolution was determined using the procedure described in another work³². Depending on the number of signals, the revolution times of individual ions are typically determined with sub-picosecond precision. All the individual revolution times were put into a histogram forming an integrated time spectrum (Fig. 3a). The measured spectrum was compared with the one simulated according to equation (1) (ref. 73). Since the pattern of mass-to-charge ratios is unique, unambiguous particle identification was achieved.

$B\rho$ -IMS technique

The modification of the present technique^{33,34}, compared with conventional IMS^{29,30}, is the enabled velocity measurement for each stored ion. The momentum of a particle, p , with mass m and velocity v is defined as $p = mv\gamma$, where $\gamma = 1/\sqrt{1 - v^2/c^2}$ is the relativistic Lorentz factor and c is the speed of light in a vacuum. Numerous fragments are produced in the nuclear reaction and their relative momentum distributions are a few per cent broad⁵. Therefore, many different

combinations of mass-to-charge ratios and velocities match the magnetic rigidity of $B\rho = mv\gamma/q = 5.528 \text{ Tm}$ of the RIBLL2–CSRe system. However, the isochronous condition is satisfied only for particles with $\gamma = \gamma_i = 1.352$ (equation (1)), defining the centre of the isochronous window. The attainable mass-resolving power rapidly deteriorates outside of the isochronous window^{26,27,43,74,75}. By obtaining the information on the velocity of every stored ion at each revolution, we are now able to correct for ‘non-isochronicity’ effects. As a result, we succeeded in improving the mass-resolving power in the isochronous window by about a factor of 2. Furthermore, this high mass-resolving power is maintained for the entire set of measured nuclei. The standard deviation of the peaks in the spectrum shown in Fig. 3a is about 1 ps, which can be translated to m/q spreads of about $5/q$ keV. For our mass measurements in the $A \approx 65$ and $Z \approx 33$ region, this corresponds to the mass-resolving power of about 160,000 (full-width at half-maximum) (refs. 33,34).

The achieved improvements boost the sensitivity, efficiency and precision of the IMS and are decisive to enable mass measurements on the very rare species reported here.

By knowing the revolution time T and velocity v of every ion, magnetic rigidity $B\rho$ and orbit length C can be straightforwardly determined via

$$B\rho = \frac{m}{q} \gamma v \quad (5)$$

and

$$C = Tv. \quad (6)$$

Since the particles with the same $B\rho$ must have the same mean C , a universal dependence, that is, $B\rho(C)$, can be constructed, which is valid for all the ions.

By using nuclei with well-known masses ($\sigma < 5$ keV), the correspondence of $B\rho$ to C has been determined. We note that the reference masses typically belong to not very exotic nuclear species and are thus abundant in the spectrum (Fig. 3a). Therefore, the calibration $B\rho(C)$ function is statistically solid and robust. Every unknown mass-to-charge ratio $(m/q)_i$ can then be derived via

$$\left(\frac{m}{q}\right)_i = \frac{B\rho(C)_i}{(\gamma v)_i}, \quad (7)$$

where index i runs over all the nuclear species of interest. Equation (7) is the basic formula of $B\rho$ -IMS (refs. 33,34).

Mass of ⁶⁶Se

The mass-to-charge ratios of ⁶⁶Se³⁴⁺ and ³³Cl¹⁷⁺ are nearly identical. Their revolution time distributions completely overlap. To obtain the m/q value of ⁶⁶Se, we utilized the dependence of timing-signal amplitudes on the ion charge⁴¹. The ions with a larger charge cause, on average, more electrons to be emitted from the foil surface, and thus, the amplitudes of the individual signals increase with the ion charge. We introduced a charge-dependent parameter U defined as

$$U = \epsilon \times \bar{A} = \frac{\sum A_i}{N}, \quad (8)$$

where ϵ is the detection efficiency for a specific ion, \bar{A} is the average amplitude of the timing signals, N is the number of accomplished revolutions and A_i is the amplitude of each timing signal. Index i runs over all the timing signals for this specific ion. A scatter plot of U versus m/q is shown in Fig. 3c. The group of counts corresponding to ⁶⁶Se³⁴⁺ can be clearly separated from the ones for ³⁷Cl¹⁷⁺ (Fig. 3b), and hence, the mass-to-charge ratio can be precisely determined.

Multizone X-ray burst model

Spherically symmetric multizone model calculations of type-I X-ray bursts were performed with modules for experiments in stellar astrophysics (MESA) (refs. 76–79) having code version 9793. The model consists of a 0.01-km-thick envelope segmented into ~1,000 zones, which adapts over the calculation. The lower boundary of the envelope is heated with 0.1 MeV per accreted nucleon and has a surface gravity corresponding to a typical neutron star with mass $M_{\text{NS}} = 1.4M_{\odot}$ and radius $R_{\text{NS}} = 11.2$ km. The key microphysics in the calculations include a general relativistic correction to the local gravity of each zone⁷⁸, a time-dependent mixing-length theory approximation for convection^{76,80}, OPAL type-2 opacities⁸¹ based on a 2% metallicity Z assuming the solar metal distribution in ref. 82 and ReacLib version 2.2 nuclear reaction rate library⁸³ using the 304 isotope network of ref. 11. Nuclear masses from AME20 (ref. 36) were used, except for the calculations performed with the nuclear masses newly determined in the present work. Time and spatial resolution settings are as described elsewhere¹⁷.

Accretion onto the neutron-star surface was modelled by continually adding material to the surface zone, which, in this case, consisted of hydrogen mass fraction $X = 0.75$, $Z = 0.02$ and helium mass fraction $Y = 1 - X - Z$, where accreted metals were distributed according to another work⁸², at an accretion rate of $2.98 \times 10^{-9} M_{\odot} \text{ yr}^{-1}$. These correspond to the conditions found elsewhere¹⁷ to best reproduce the year 2007 bursting epoch of the ‘clock burster’ GS 1826–24 (refs. 45–47), although with a larger X , which was found to improve agreement with observations when using a finer grid of astrophysical conditions¹⁹.

X-ray burst light curves (Fig. 4) were calculated by stacking, averaging and smoothing the surface luminosity output from MESA, whereas the uncertainty bands were statistically calculated, as described in detail elsewhere¹⁷. To mitigate the effects of compositional inertia⁸⁴, the first several bursts calculated in the bursting sequence were not included in the light curve calculation.

X-ray burst abundance distributions (‘ashes’) were calculated following the burst sequence by determining the mass fraction of species in the region of the envelope that is above the original substrate and below the zones experiencing hydrogen and helium burning^{52,57,60}.

The optimum distance and surface gravitational redshift ($1+z$) for reproducing the observed light curve of the year 2007 bursting epoch of GS 1826–24 was determined by performing light-curve shape comparisons for a grid of distances and $(1+z)$. As described elsewhere^{17,57}, the confidence intervals are determined by calculating χ^2 for each distance and $(1+z)$ in the grid and taking the difference between this and the minimum χ^2 in the phase space, following the approach detailed elsewhere⁸⁵.

Data availability

Datasets of the simulated light curves and ash distributions used to create Fig. 4 are available via Zenodo at <https://zenodo.org/record/7427118#.ZBD7Wy8w2gQ> (ref. 61). Raw data from the mass measurement experiment in CSRe are available from the corresponding authors on request.

Code availability

MESA is provided elsewhere⁷². Codes employed for the data processing and analysis of mass measurements in CSRe are available from the corresponding authors on request.

References

67. Yan, X.-L. et al. Characterization of a double time-of-flight detector system for accurate velocity measurement in a storage ring using laser beams. *Nucl. Instrum. Meth. Phys. Rev. A* **931**, 52–59 (2019).
68. Shuai, P. et al. An improvement of isochronous mass spectrometry: velocity measurements using two time-of-flight detectors. *Nucl. Instrum. Meth. Phys. Rev. B* **376**, 311–315 (2016).

69. Xing, Y. M. et al. First isochronous mass measurements with two time-of-flight detectors at CSRe. *Phys. Scr.* **2015**, 014010 (2015).
70. Xu, X. et al. A data analysis method for isochronous mass spectrometry using two time-of-flight detectors at CSRe. *Chinese Phys. C* **39**, 106201 (2015).
71. Zhang, W. et al. Time-of-flight detectors with improved timing performance for isochronous mass measurements at the CSRe. *Nucl. Instrum. Meth. Phys. Rev. A* **756**, 1–5 (2014).
72. Zhang, W. et al. A timing detector with pulsed high-voltage power supply for mass measurements at CSRe. *Nucl. Instrum. Meth. Phys. Rev. A* **755**, 38–43 (2014).
73. Xing, Y. M. et al. Particle identification and revolution time corrections for the isochronous mass spectrometry in storage rings. *Nucl. Instrum. Meth. Phys. Rev. A* **941**, 162331 (2019).
74. Geissel, H. & Litvinov, Y. A. Precision experiments with relativistic exotic nuclei at GSI. *J. Phys. G: Nucl. Part. Phys.* **31**, 1779–1783 (2005).
75. Yamaguchi, T., Koura, H., Litvinov, Y. A. & Wang, M. Masses of exotic nuclei. *Prog. Part. Nucl. Phys.* **120**, 103882 (2021).
76. Paxton, B. et al. Modules for experiments in stellar astrophysics (MESA). *Astrophys. J. Suppl. Ser.* **192**, 3 (2011).
77. Paxton, B. et al. Modules for experiments in stellar astrophysics (MESA): planets, oscillations, rotation, and massive stars. *Astrophys. J. Suppl. Ser.* **208**, 4 (2013).
78. Paxton, B. et al. Modules for experiments in stellar astrophysics (MESA): binaries, pulsations, and explosions. *Astrophys. J. Suppl. Ser.* **220**, 15 (2015).
79. Modules for Experiments in Stellar Astrophysics (MESA); <https://docs.mesastar.org>
80. Henyey, L., Vardya, M. S. & Bodenheimer, P. Studies in stellar evolution. III. The calculation of model envelopes. *Astrophys. J.* **142**, 841–854 (1965).
81. Iglesias, C. A. & Rogers, F. J. Radiative opacities for carbon- and oxygen-rich mixtures. *Astrophys. J.* **412**, 752–760 (1993).
82. Grevesse, N. & Sauval, A. J. Standard solar composition. *Space Sci. Rev.* **85**, 161–174 (1998).
83. Cyburt, R. H. et al. The JINA REACLIB database: its recent updates and impact on type-I X-ray bursts. *Astrophys. J. Suppl. Ser.* **189**, 240–252 (2010).
84. Woosley, S. E. et al. Models for type I X-ray bursts with improved nuclear physics. *Astrophys. J. Suppl. Ser.* **151**, 75–102 (2004).
85. Press, W. H., Teukolsky, S. A., Vetterling, W. T. & Flannery, B. P. *Numerical Recipes in C: The Art of Scientific Computing* 2nd edn (Cambridge Univ. Press, 1992).

Acknowledgements

We thank the staff of the accelerator division of IMP for providing a stable beam. This work is supported by the National Key R&D Program of China through grant no. 2018YFA0404401 to Y.H.Z., M.W., Y.M.X., M.Z., M.Z.S. and X.Z.; the Strategic Priority Research Program of the Chinese Academy of Sciences through grant no. XDB34000000 to Y.H.Z. and M.W.; the CAS Project for Young Scientists in Basic Research through grant no. YSBR-002 to M.W. and X.L.Y.; the National Key Research and Development (R&D) Program under grant no. 2021YFA1601500 to Y.F.N., W.J.H. and M.Z.; the National Natural Science Foundation of China through grant no. 12135017 (Y.H.Z.), no. 12121005 (X.H.Z., Y.H.Z. and M.W.), no. 11961141004 (M.W.), no. 11905259 (C.Y.F.), no. 11905261 (Y.M.X.), no. 11975280 (X.X.), no. 12105333 (W.W.G.) and nos. 11835001, 11921006 and 12035001 (F.R.X.); the CAS Light of West China Program to Y.M.X. and C.Y.F.; the CAS Young Scholar of Regional Development through grant no. 15[2023] to X.L.Y.; the State of Hesse within the Research Cluster ELEMENTS through project ID 500/10.006 to Y.A.L.; the Youth Innovation Promotion Association

of the Chinese Academy of Sciences through grant no. 2019406 to S.Q.H.; the US Department of Energy, Office of Science, through grant nos. DE-FG02-88ER40387 and DE-SC0019042 to Z.M.; the US National Nuclear Security Administration through grant nos. DE-NA0003883 and DE-NA0003909 to Z.M.; the US National Science Foundation through grant nos. PHY-1430152 and OISE-1927130 to Z.M.

Author contributions

X.Z., M.W., Y.H.Z., X.H.Z., S.Q.H., K.A.L., H.S.X., R.J.C., H.Y.D., C.Y.F., W.W.G., J.J.H., W.J.H., H.Y.J., H.F.L., J.G.L., T.L., S.A.L., M.L.L., P.S., J.Y.S., Y.N.S., M.Z.S., Q.W., Y.M.X., X.X., X.L.Y., J.C.Y., Y.Y., Y.J.Y., Q.Z., M.Z. and S.Z. performed the experiment. X.Z., M.W., Y.H.Z., Y.A.L. and X.H.Z. performed the data analysis. Y.F.N., F.R.X. and Q.Y. provided the theory support. Z.M. performed the X-ray burst simulations. X.Z., M.W., Y.H.Z., Y.A.L., Z.M., K.B., X.H.Z. and F.R.X. prepared the manuscript. All the

authors discussed the results and contributed to the manuscript at all the stages.

Competing interests

The authors declare no competing interests.

Additional information

Correspondence and requests for materials should be addressed to M. Wang, Y. H. Zhang or Yu. A. Litvinov.

Peer review information *Nature Physics* thanks Nobuya Nishimura and the other, anonymous, reviewer(s) for their contribution to the peer review of this work.

Reprints and permissions information is available at www.nature.com/reprints.